Current Overshoot Suppression of Wireless Power Transfer Systems With ON–OFF Keying Modulation

Wenxing Zhong, *Member, IEEE*, Hao Li, S. Y. R. Hui, *Fellow, IEEE*, and Mark Dehong Xu, *Fellow, IEEE*

***Abstract*—The energy efficiency of an inductive wireless power transfer (WPT) system will deviate from the possible peak value if the magnetic coupling of the transmitter and receiver coils or the load resistance changes. To achieve maximum-efficiency tracking regardless of coupling or load changes, ON–OFF keying (OOK) modulation is used. However it has the issue of large surge current in the circuits during OOK modulation. The current overshoots of a series–series (SS) compensated WPT system at the startup stage might be much higher than the rated current. The current overshoots not only increase the stress on the power switch devices but also cause high voltage spikes across the windings and the resonant capacitors which is a challenge for insulation design. A soft-start scheme is proposed to address the current overshoot problem. The principle of the soft-start scheme can be essentially applied to WPT systems with different compensation topologies. The experimental results of a 3.3-kW prototype verify that the proposed soft-start scheme effectively suppress the current overshoots.**

***Index Terms*—Inductive power transfer, on-off keying modulation, wireless power transfer.**

I. Introduction

INDUCTIVE resonant coupling has been widely adopted as the wireless charging technique for portable electronics and electric vehicles (EV) [1]. In an inductive wireless charging system, the load resistance varies in a large range as the battery voltage and charging current change in the charging process [2]. The energy efficiency of an inductive wireless charging system strongly depends on the load resistance [3]. As a result, the charging efficiency could be very low under light-load condition and thus, the overall energy efficiency of the system is degraded. Many efforts have been devoted to techniques that can enable maximum-efficiency operation for an inductive wireless power transfer (WPT) system. Maximum-efficiency operation means the efficiency of the system will maintain at a value close to the maximum possible efficiency of the system in the entire charging process regardless of the variation of load resistance or coupling.

Manuscript received February 26, 2020; revised May 1, 2020 and June 21, 2020; accepted July 25, 2020. Date of publication August 3, 2020; date of current version October 30, 2020. This work was supported by the National Natural Science Foundation of China under Grant 51807174. Recommended for publication by Associate Editor M. Ponce-Silva. (*Corresponding author: Mark Dehong Xu.*)

Wenxing Zhong, Hao Li, and Mark Dehong Xu are with the Institute of Power Electronics, Zhejiang University, Hangzhou 310027, China (e-mail: wxzhong@zju.edu.cn; 21710122@zju.edu.cn; xdh@zju.edu.cn).

S. Y. R. Hui is with the Department of Electrical and Electronic Engineering, The University of Hong Kong, Hong Kong, and also with the Imperial College London, London SW7 2AZ, U.K. (e-mail: ronhui@eee.hku.hk).

Color versions of one or more of the figures in this article are available online at https://ieeexplore.ieee.org.

Digital Object Identifier 10.1109/TPEL.2020.3012949

A dc/dc converter can be used after the rectifier in the secondary circuit to transform the load resistance and maximize power transfer efficiency [3]–[13]. For light-load conditions, boost-type converters can be used to convert the load resistance to the optimal value [14]–[24]. Reconfigurable resonant circuits can also be used to match the load impedance. In [25], a switchable capacitor array is used for impedance matching, while [26] uses a set of switchable coils. In [27], a reconfigurable coil structure which can operate in either two-coil or three-coil mode is proposed and the system efficiency can stay close to the maximum within a large range of load resistance.

Burst-mode control has been widely adopted in power converters to improve the light-load efficiency [29]–[34]. It is capable of setting the equivalent load of light-load conditions equal to that of full-load or optimal-load conditions [28], [35], [36]. This function of burst-mode control is especially useful for WPT systems whose efficiency has a much stronger dependency on the load compared with usual power converters [3]. In [35], a harmonic burst control is proposed for inductive WPT systems to regulate the output power through harmonics and it can achieve both turn-ON and turn-OFF soft switching for a wide range of loads. In [28], burst-mode control WPT, which is called OOK modulated WPT in the paper, is investigated from the perspective of achieving maximum light-load efficiency. The optimal input voltage and the maximum-efficiency operation mechanism of OOK WPT are derived. In [36], a dual-side control WPT system with a burst-mode secondary is proposed. Burst-mode operation in this method is not only for regulating the output but also for creating a feedback signal for the primary controller.

Maximum-efficiency operation techniques, which utilize extra circuit or components not only increase the complexity of the system but also power losses. Burst-mode control (or OOK modulation) without using any extra circuit or component is a promising alternative. The schematic of the OOK WPT system proposed in [28] is redrawn in Fig. 1. A low-frequency modulation signal S_{LF} is used to modulate the switching actions and the equivalent load resistance is a function of the duty cycle of the modulation signal. This mechanism of OOK modulation is capable of improving the efficiency of WPT systems not only under light-load conditions as reported in [28] but also with a large coupling range. Moreover, since a low power level is used in [28], the current overshoots created in the turn-ON transient processes have not been revealed. In the switching power supply, burst mode generally is enabled at light-load condition. However for the wireless charging system, it operates at wide load and coupling ranges. The current overshoots of a WPT system at

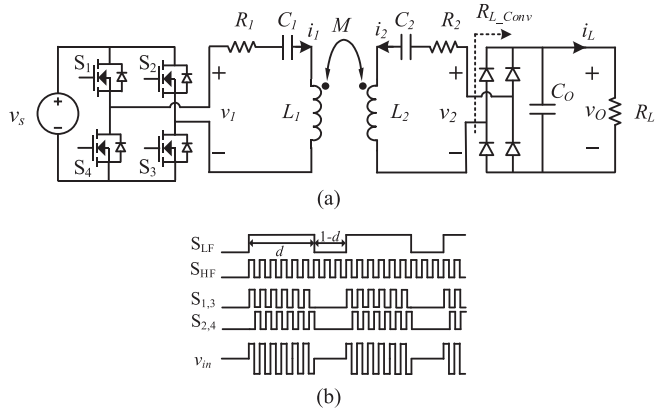

Fig. 1. Schematic of an SS OOK WPT system. (a) Schematic of the system. (b) Switching signals for the inverter [28].

the startup stage might be much higher than the rated current. The current overshoots not only increase the stress on the power switch devices but also cause dangerous high voltage spikes across the windings and the resonant capacitors. It will become more serious when the power level goes higher, e.g., in an EV wireless charging system.

In this article, a revised OOK method with a soft-start scheme is proposed. The soft-start scheme enables a fast turn-ON transient process without causing significant current overshoots. In addition, a design of the soft-start scheme is also presented. The proposed soft-start scheme is verified with both the simulation and experiment. The principle of the proposed soft-start scheme can be extended to other WPT systems with different compensation topologies.

The rest of article is organized as follows. Section I introduces the background of the article. In Section II, the features of the OOK modulation for WPT systems are briefly reviewed. Especially, current overshoot issue in OOK WPT is investigated. In Section III, a soft-start scheme is presented for OOK WPT. In Section IV, the soft-start scheme is verified by the simulation. In Section V, experimental results are given to verify the analysis and the proposed soft-start scheme.

II. Features of OOK WPT

A. Efficiency Improvement and Output Regulation

OOK modulation is basically a burst mode control method. By operating the system at rated power in each ON period, the winding efficiency can be improved [28]. The equivalent load resistance is given by the following equation for an SS OOK WPT system [28]

$$R_{L\_Conv} = d\frac{8}{\pi^2}R_L \tag{1}$$

where *d* is the duty cycle of the low-frequency modulation signal as shown in Fig. 1, and R_L is the load resistance.

The optimal load resistance of an SS WPT system to achieve maximum efficiency is given by

$$R_{L\_OPT} = R_2\sqrt{1+\frac{\omega^2M^2}{R_1R_2}} = R_2\sqrt{1+k^2Q_1Q_2} \tag{2}$$

where R_1 and R_2 are the parasitic resistance of the primary and secondary *LC* resonators, respectively; *M* is the mutual inductance of the windings, ω is the angular frequency, and Q_1 and Q_2 (defined as $Q_i = \omega L_i/R_i, i = 1$ or 2, L_i is the self-inductance of winding-*i*) are the quality factors of the primary and secondary resonators, respectively.

Since $k^2Q_1Q_2$ is normally much larger than 1, (2) can be simplified to

$$R_{L\_OPT} = kR_2\sqrt{Q_1Q_2}. \tag{3}$$

Assume the system can achieve maximum efficiency with a coupling coefficient of k_0 and a load resistance of R_{L0}

$$\text{for } k_0 \text{ and } R_{L0}\text{: } d_0\frac{8}{\pi^2}R_{L0} = k_0R_2\sqrt{Q_1Q_2}. \tag{4}$$

Then when with an arbitrary *k* and an arbitrary R_L, the duty cycle *d* that can convert R_L to the optimal value is given by

$$\text{for } k \text{ and } R_L\text{: } d\frac{8}{\pi^2}R_L = kR_2\sqrt{Q_1Q_2}. \tag{5}$$

From these two equations, we can get

$$d = d_0\frac{kR_{L0}}{k_0R_L}. \tag{6}$$

From the aspect of output regulation, the required duty cycle for maintaining a constant output voltage under load and coupling changes can also be derived. In an SS WPT system, when the parasitic resistances are neglected, we have

$$\omega MI_2 = V_1 \tag{7}$$

$$\omega MI_1 = V_2. \tag{8}$$

Note that the italic symbols represent rms values. At the operation point with k_0 and R_{L0}, the energy delivered to the secondary side in one ON period of OOK should be equal to the total output energy in one ON-and-OFF period of OOK

$$d_0\frac{2\sqrt{2}}{\pi}I_2V_O = \frac{V_O^2}{R_{L0}}. \tag{9}$$

By combining (7) and (9)

$$d_0 = \frac{\pi}{2\sqrt{2}}k_0\frac{V_O\omega\sqrt{L_1L_2}}{V_1R_{L0}}. \tag{10}$$

Similarly, when with an arbitrary *k* and R_L, we have

$$d' = \frac{\pi}{2\sqrt{2}}k\frac{V_O\omega\sqrt{L_1L_2}}{V_1R_L}. \tag{11}$$

By comparing (10) and (11)

$$d' = d_0\frac{kR_{L0}}{k_0R_L}. \tag{12}$$

So (6) and (12) are the same, which implies that applying OOK modulation for constant output voltage regulation is able to achieve a higher efficiency, regardless of coupling changes.

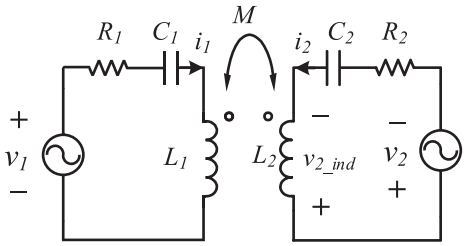

Fig. 2. First-order circuit model of the WPT system with a constant output voltage.

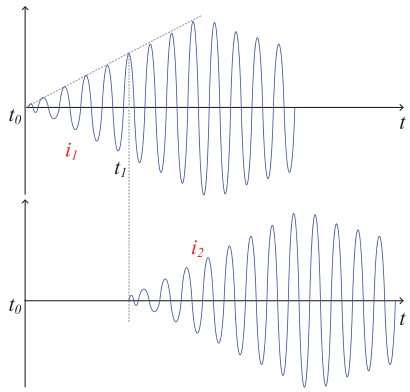

Fig. 3. Primary and secondary current waveforms at the startup stage [not to scale].

B. Current Overshoots of SS WPT

A major challenge of OOK modulation is its transient process at the startup stage in each ON period. At the startup stage of each ON period of OOK, there will be large current overshoots in both primary and secondary circuits due to the nature of high-Q resonant circuits. The system is assumed to have a constant output voltage in the interested time span, which is valid for battery charging applications. As shown in Fig. 2, v_2 represents the fundamental component of the rectifier input voltage in the secondary side circuit. Assume the constant output voltage is V_O, then the amplitude of v_2 is given by

$$V_{2m} = \frac{4}{\pi} V_O. \tag{13}$$

When the inverter is turned ON at the beginning of an ON period of OOK (at time t_0), the primary current starts to rise. But the secondary current will be zero until the primary current is large enough to induce a voltage in the secondary winding higher than the output voltage. Use t_1 to denote the moment when the secondary current starts to increase. The primary and secondary currents will have the pattern, as shown in Fig. 3, at the startup stage. From t_0 to t_1, the secondary current is zero and thereby, the primary circuit is a series RLC second-order circuit. The source is

$$v_1(t) = V_1 \sin \omega t. \tag{14}$$

The initial capacitor voltage is V_{C10} and the initial inductor current is zero. It should be noted that V_{C10} could be any value between zero and the dc input voltage of the inverter and it depends on the time when the ON period ends. Therefore

$$V_{C10} \le \frac{\pi}{4} V_1. \tag{15}$$

Use V_{C1S} to denote the steady-state capacitor voltage which is given by

$$V_{C1S} = \frac{V_1}{R_1} \cdot \frac{1}{\omega C_1} = Q_1 V_1. \tag{16}$$

Therefore

$$V_{C1S} >> V_{C10}. \tag{17}$$

Define

$$\alpha = \frac{R_1}{2L_1} \tag{18}$$

$$\omega_\alpha^2 = \omega^2 - \alpha^2 = \omega^2 \left[1 - \left(\frac{1}{2Q_1}\right)^2\right] \approx \omega^2. \tag{19}$$

Then based on the basic theory of second-order circuit, the time-domain current function can be derived as

$$i_1(t) = \omega C_1 \left[V_{C1S} - \left(1 + \frac{1}{4Q_1^2}\right)(V_{C10} + V_{C1S})\, \mathrm{e}^{-\alpha t}\right] \sin \omega t. \tag{20}$$

Considering (17) and Q_1 is usually larger than 100, (20) can be simplified to

$$i_1(t) = \omega C_1 V_{C1S} \left(1 - \mathrm{e}^{-\alpha t}\right) \sin \omega t. \tag{21}$$

Define

$$I_1(t) = \omega C_1 V_{C1S} \left(1 - \mathrm{e}^{-\alpha t}\right) \tag{22}$$

which represents the increasing amplitude of $i_1(t)$.

The induced voltage in the secondary winding can be derived as

$$M \frac{di_1}{dt} \approx \omega M I_1(t) \cos \omega t. \tag{23}$$

The proof of (23) is given in the Appendix.

In summary, after the primary-side inverter is activated, it takes some time for the secondary-side *LC* resonator to create a voltage higher than the output voltage so that it can gradually built up a current. In this time period, the primary-side *LC* resonator, whose damping factor is negligibly small, generates an oscillating current with a fast increasing amplitude. Thereby, large current overshoots appear and these current overshoots will also induce large current oscillations in the secondary side. With a weaker coupling, the current overshoots will be more serious. The large current overshoots not only increase the ratings of the components and windings but also cause high voltage spikes across the windings and the resonant capacitors which is a challenge for insulation design.

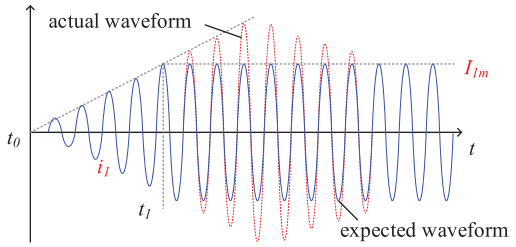

Fig. 4. Expected primary current.

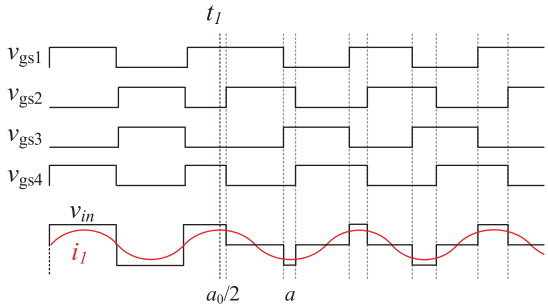

Fig. 5. Schematic diagram of the modulation signals and the inverter output voltage.

III. Soft Start Scheme

This section introduces a soft start scheme to eliminate current overshoots at the startup stage. Meanwhile, minimal transient time is ensured. The condition of the induced voltage in the secondary winding is larger than the output voltage is equivalent to

$$\omega M I_1(t)\cos\omega t > \frac{4}{\pi}V_O. \tag{24}$$

Considering (8), (24) leads to

$$I_1(t) > \frac{4}{\pi}\frac{V_O}{\omega M} \approx I_{1m} \tag{25}$$

where I_{1m} is the steady-state primary current considering the whole WPT system. This implies that at t_1 when the secondary current starts to rise, the amplitude of the primary current should be larger than the steady-state current. By properly controlling the input voltage v_1 (e.g., by adjusting the phase shift of the inverter legs), the transition time t_1 can be located at the time when $i_1(t)$ peaks (i.e., $I_1(t_1) = I_{1m}$).

The expected primary current waveform is shown in Fig. 4 . The primary current increases normally from t_0 to t_1 and then it enters steady state at t_1. Note that t_1 is the time when the secondary current starts to increase. Therefore, if one could modulate the inverter output from t_1 in a way that v_1 exactly equals to the sum of the voltage of R_1 and the voltage induced by i_2, then L_1 and C_1 will keep resonant with the same amplitude and thereby, i_1 will maintain at $I_{1\mathrm{m}}$ from t_1. Setting t_1 to time zero, the primary current is given by

$$i_1(t) = I_{1m}\cos\omega t \tag{26}$$

TABLE I
Parameters of the Charging System with Perfect Coupling

Symbol	Aligned	90 mm misaligned
L_1	489 uH	494 uH
C_1	7.12 nF	7.12 nF
R_1	0.94 Ω	0.94 Ω
L_2	494 uH	499 uH
C_2	7.19 nF	7.19 nF
R_2	0.91 Ω	0.91 Ω
M	65.3 uH	43.4 uH
k	0.133	0.087

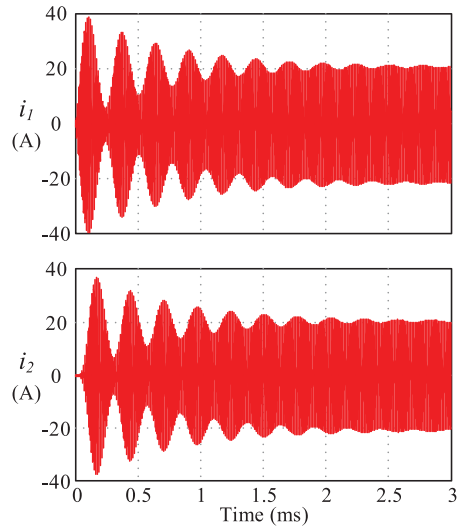

Fig. 6. Simulation results of current overshoots without using the soft-start scheme.

and the required input voltage is given by

$$v_1(t) = M\frac{di_2}{dt} + R_1 I_{1m}\cos\omega t. \tag{27}$$

Assume the condition of (27) can be practically realized. The primary current enters steady state from t_1, which implies that the induced voltage in the secondary winding is a constant sinusoidal voltage source which is given by

$$v_{2\_ind}(t) = -M\frac{di_1}{dt} = \omega M I_{1m}\sin(\omega t). \tag{28}$$

Thereby, the secondary circuit can be considered as a second-order series RLC resonant circuit with a sinusoidal voltage source which is the sum of the induced voltage and the fundamental component of the rectifier input voltage, and zero initial conditions. It can be proved that the induced voltage and the fundamental output voltage are basically in phase under the condition of using high-Q resonators. The proof is given in the appendix. Similar to (23) and assuming identical resonators are used in both the primary and secondary sides, the secondary current is given by

$$i_2(t) = \omega C_2 V_{C2S}\left(1 - \mathrm{e}^{-\alpha t}\right)\sin\omega t. \tag{29}$$

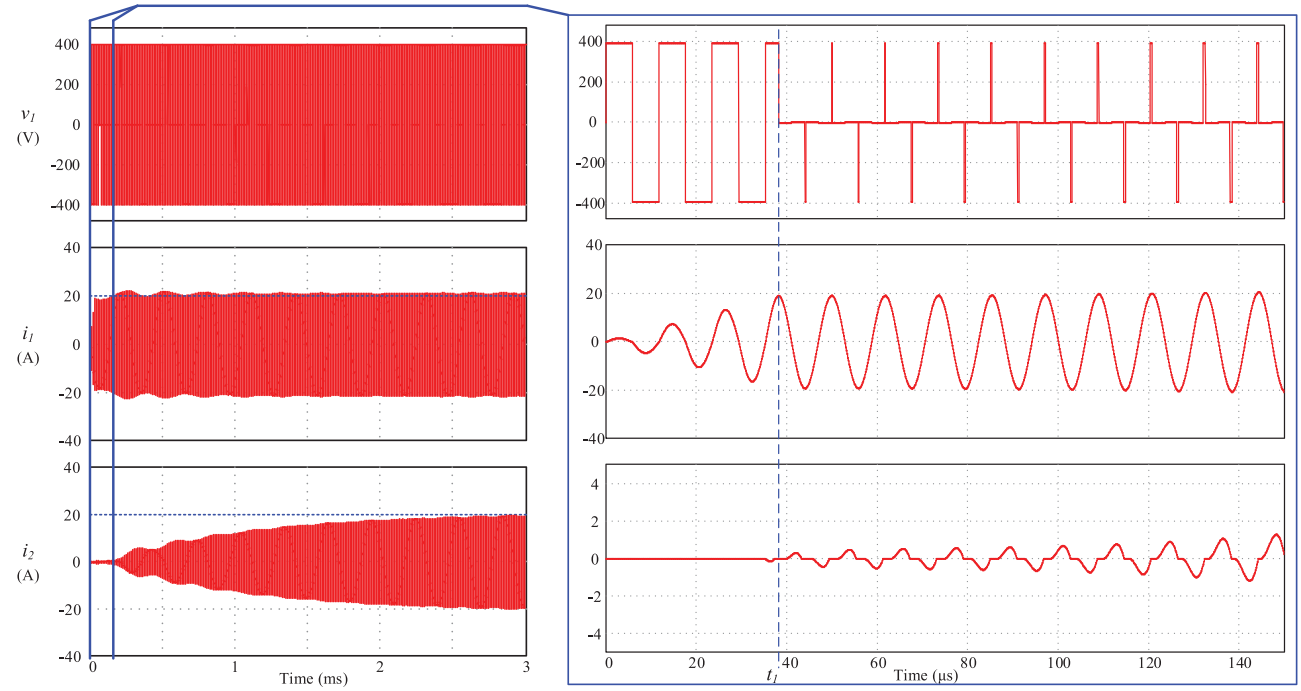

Fig. 7. Simulation results after applying the soft-start scheme.

It should be noted that the zero time for $i_2(t)$ is set at t_1 and the zero time for $i_1(t)$ in (21) is t_0.

Use $a(t)$ to denote the phase shift between the two inverter legs, the fundamental output voltage of the inverter is

$$v_1(t) = V_S \frac{4}{\pi} \sin\left[\frac{a(t)}{2}\right] \cos \omega t. \tag{30}$$

By solving (27) and (30)

$$a(t) = 2 \arcsin\left(\frac{\pi}{4} \frac{I_{1m} R_1 + \omega^2 M C_2 V_{C2S} \left(1 - \mathrm{e}^{-\alpha t}\right)}{V_S}\right) \tag{31}$$

where

$$V_{C2S} = \frac{I_{2m}}{\omega C_2} \tag{32}$$

is the steady-state amplitude of the capacitor voltage and I_{2m} is given by (7).

Fig. 5 shows the schematic diagram of the modulation, where a_0 is the initial value of the phase shift angle when the modulation starts. However, because the modulation starts at the maximum current point (i.e., time t_1), half of a_0 can be considered to have overlapped with the previous ON period and only half of a_0 is needed after t_1.

IV. Simulation Verification

A circuit simulation has been carried out to verify the proposed soft-start scheme. Take the system at the worst coupling position (measured parameters given in Table I) as an example. The steady-state primary and secondary currents (i.e., I_{1m} and I_{2m}) are 19.8 and 21.7 A according to (8) and (7), respectively. In the simulations, it is assumed that the output voltage is fixed at 360 V and lossless switches are used. If the proposed soft-start scheme is not applied, the maximum currents at the startup stage are nearly twice the stead-state values as shown in Fig. 6.

By setting (22) equal to I_{1m}, the time when the amplitude of i_1 reaches I_{1m} can be obtained as 39.29 μs. On the other hand, it takes 38.24 μs for the inverter output voltage to complete 3.25 cycles at 85 kHz. Therefore, the modulation time t_1 can be set at 3.25 cycles. After t_1, the driving signals of the inverter are modulated so that the inverter output voltage has an increasing duty cycle corresponding to the phase given by (31). The simulation results are given in Fig. 7. The current overshoots have been significantly eliminated. The steady-state primary current is slightly higher than the calculated value because the winding resistances are included in the simulations.

V. Experimental Verification

Magnetic couplers have been constructed using the common coil-ferrite-shield three-layer structure [37] for experiments, as shown in Fig. 8. Strip-shape ferrite layer is adopted. The parameters of the setup is given in Table I for the perfect-coupling position and the misaligned position with a 90-mm lateral misalignment. Fig. 9 shows the primary circuit of the prototype. SiC MOSFET C2M0025120D is used in the full-bridge inverter and the microprocessor is DSP2808. Fast switching diode IDW100E60 is used for the rectifier. The input dc-link voltage is 395 V and the dc output voltage is 360 V. The rated output power is 3.3 kW.

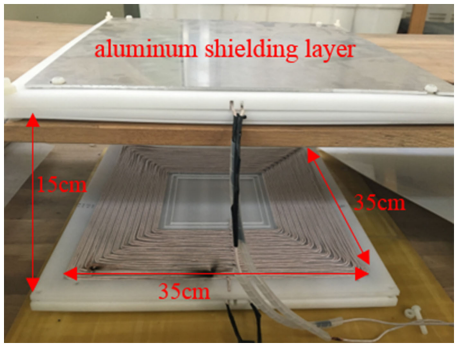

Fig. 8. Couplers of the prototype WPT system.

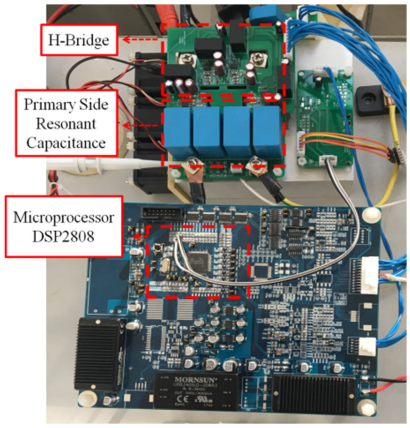

Fig. 9. Primary-side circuit.

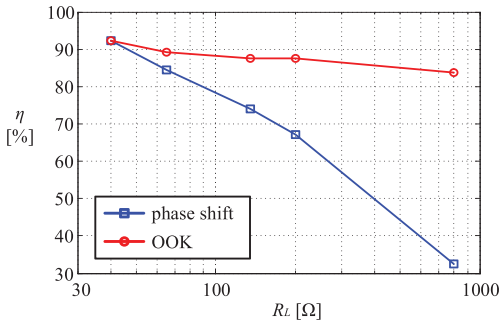

Fig. 10. Efficiencies at the best-coupling position ($k = 0.133$).

A. Efficiency Improvement

The measured dc-to-dc efficiencies of the prototype WPT system of using OOK modulation and phase-shift control are compared, at both the best-coupling and misaligned positions, as shown in Figs. 10 and 11, respectively. Significant efficiency improvements are obvious for larger load resistances, especially at the misaligned position.

B. Simultaneous Maximum-Efficiency Operation and Output Voltage Regulation

The calculated OOK duty cycles according to (6) and (12) are compared with the actual used values in experiments for regulating a constant output voltage. They are in good agreement as shown in Fig. 12.

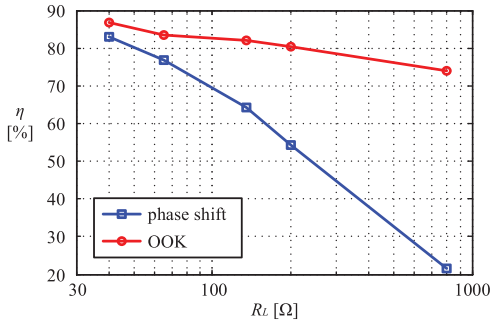

Fig. 11. Efficiencies at the worst coupling position ($k = 0.087$).

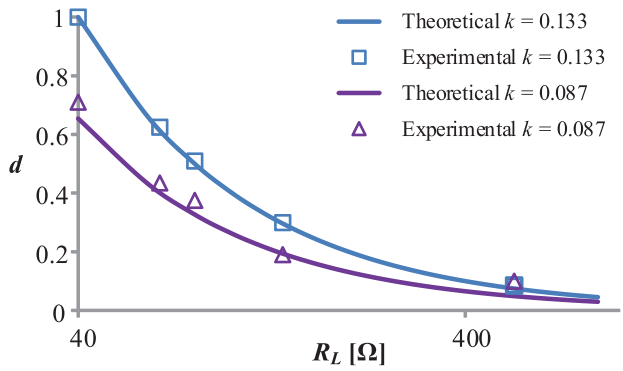

Fig. 12. OOK duty cycle at the best-coupling and misaligned positions.

C. Current Overshoots Suppression

According to (25), the steady-state amplitude of the primary current is 13.1 A for the best-coupling position and 19.8 A for the misaligned position. Similar to the simulation, the soft-start modulation starting time, i.e., t_1, can be obtained using (22) and the phase shift of the inverter legs is given by (31). The experimental results under half load are given in Table II. The current overshoots are effectively eliminated by applying the soft-start scheme at both the best-coupling position and the misaligned position.

With the soft-start scheme, the increasing rate of the secondary current will inevitably become slower and thereby the OOK duty cycle will be increased to support the same output voltage and output power. This will degrade the efficiency. Therefore, a tradeoff should be made between efficiency and current overshoot. For example, in the third column of Table II, the increasing rating of the phase shift is increased by 50% compared to that in the middle column with a phase shift given by (31). Thereby, the transient time of the currents will become shorter and the efficiency can be improved. However, this leads to a bit higher maximum currents.

TABLE II
EXPERIMENTAL RESULTS OF CURRENT OVERSHOOTS SUPPRESSION

		w/o soft start	soft start normal speed	soft start 150% speed
Best-Coupling ($k = 0.133$) Half Load	i_1	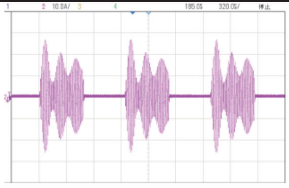 $i_{1max} = 26.8$ A	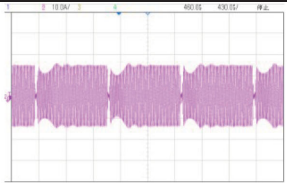 $i_{1max} = 15.5$ A	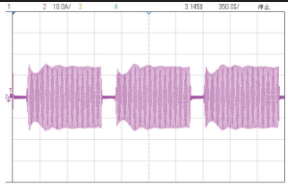 $i_{1max} = 15.3$ A
	i_2	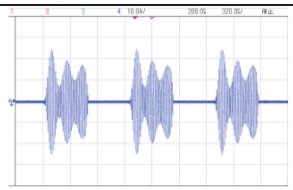 $i_{2max} = 24.5$ A	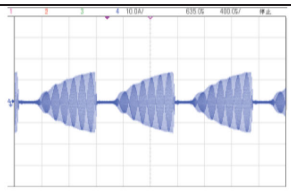 $i_{2max} = 14.0$ A	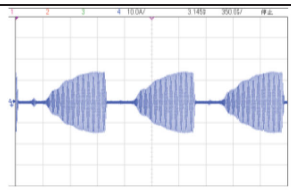 $i_{2max} = 14.0$ A
	d	0.510	0.975	0.825
	η	88.5%	87.5%	88.2%
Misaligned ($k = 0.087$) Half Load	i_1	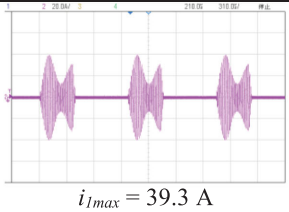 $i_{1max} = 39.3$ A	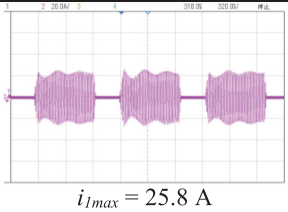 $i_{1max} = 25.8$ A	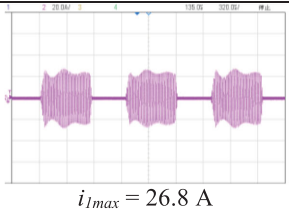 $i_{1max} = 26.8$ A
	i_2	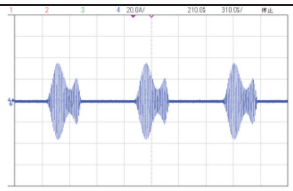 $i_{2max} = 35.3$ A	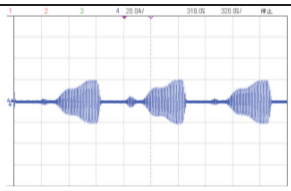 $I_{2max} = 20.3$ A	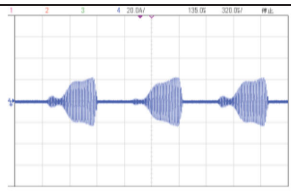 $i_{2max} = 21.8$ A
	d	0.375	0.700	0.585
	η	82.2%	80.7%	82.3%

VI. CONCLUSION

ON–OFF keying (OOK) modulation can achieve maximum-efficiency tracking regardless of coupling or load changes. However, it has the issue of large surge current in the circuits during OOK modulation. The current overshoots of a WPT system at the startup stage might be much higher than the rated current. The overshoots not only require a higher rating of the converters and resonators but also significantly increase breakdown risk. The transient response at the startup stage of the SS WPT system is analyzed based on the circuit model and a soft-start scheme for OOK WPT is proposed to suppress the current overshoots. By properly modulating the inverter output so that it balances the voltage drop across the parasitic resistance of the primary circuit and the induced voltage due to the secondary-side current, the primary *LC* resonator will resonate with a constant current amplitude, which avoids high current overshoots in the primary side and in turn also eliminate current overshoots in the secondary side. Both simulation and experimental results verify that the proposed soft-start scheme can effectively suppress the current overshoots of WPT systems.

APPENDIX

A. Proof of $M\frac{di_1}{dt} \approx \omega M I_1(t)\cos\omega t$

From the expression of $i_1(t)$ in (21), we can derive

$$M\frac{di_1}{dt} = M\omega C_1 V_{C1S}\left[(\alpha\sin\omega t - \omega\cos\omega t)\,\mathrm{e}^{-\alpha t} + \omega\cos\omega t\right]. \tag{33}$$

While

$$\frac{\alpha}{\omega} = \frac{1}{2Q_1} \tag{34}$$

which is approaching zero. Therefore, the term$\alpha\sin\omega t$ can be neglected and (33) is simplified to

$$M\frac{di_1}{dt} = M\omega^2 C_1 V_{C1S}\left(1-\mathrm{e}^{-\alpha t}\right)\cos\omega t = \omega M I_1(t)\cos\omega t. \tag{35}$$

B. Proof of The Induced Voltage in the Secondary Winding and the Fundamental Component of the Rectifier Output Voltage are in phase

Consider the fundamental component of the rectifier output voltage as a power source which has the same frequency and phase angle as the secondary current. Since the secondary resonator is also high-Q and the operating frequency of the system equals to the resonant frequency, the frequency of the transient oscillation of the secondary current will be very close to the operating frequency. Therefore, the induced voltage and the fundamental component of the rectifier output voltage can be combined and considered as one sinusoidal power source, which is represented with

$$v_{2S}(t) = V_{2S}\sin(\omega t). \tag{36}$$

Thus, the secondary current can be expressed as

$$i_2(t) = \omega C_2 V_{C2S}\left(1-\mathrm{e}^{-\alpha t}\right)\sin(\omega t) \tag{37}$$

which is similar to (21).

Similar to (35), the voltage across L_2 is derived as

$$\begin{aligned} L_2\frac{di_2}{dt} &\approx \omega^2 L_2 C_2 V_{C2S}\left(1-\mathrm{e}^{-\alpha t}\right)\cos(\omega t) \\ &= V_{C2S}\left(1-\mathrm{e}^{-\alpha t}\right)\cos(\omega t). \end{aligned} \tag{38}$$

From the basic theory of the second-order resonant circuit, the voltage of C_2 can be derived and simplified to

$$v_{C2}(t) \approx -V_{C2S}\left(1-\mathrm{e}^{-\alpha t}\right)\cos(\omega t) \tag{39}$$

Therefore, the instantaneous voltages of the winding inductance and the resonant capacitance actually cancel out and thus, the induced voltage in the secondary winding and the fundamental component of the rectifier output voltage are in phase.

REFERENCES

[1] S. Y. R. Hui, "Magnetic resonance for wireless power transfer [A look back]," *IEEE Power Electron. Mag.*, vol. 3, no. 1, pp. 14–31, Mar. 2016.

[2] Wenshuai Liao and Luis Orozco, "Accurate analog controller optimizes high-efficiency Li-ion battery manufacturing," *Analog Dialogue*, vol. 48, Aug. 2014.

[3] W. X. Zhong and S. Y. R. Hui, "Maximum energy efficiency tracking for wireless power transfer systems," *IEEE Trans. Power Electron.*, vol. 30, no. 7, pp. 4025–4034, Jul. 2015.

[4] Y. Moriwaki, T. Imura, and Y. Hori, "Basic study on reduction of reflected power using DC/DC converters in wireless power transfer system via magnetic resonant coupling," in *Proc IEEE 33rd Int. Telecommun. Energy Conf.*, Amsterdam, Netherlands, 2011, pp. 1–5.

[5] M Fu, H. Yin, X. Zhu, and C. Ma, "Analysis and tracking of optimal load in wireless power transfer systems," *IEEE Trans. Power Electron.*, vol. 30, no. 7, pp. 3952–3963, Jul. 2015.

[6] H. Li, J. Li, K. Wang, W. Chen, and X. Yang, "A maximum efficiency point tracking control scheme for wireless power transfer systems using magnetic resonant coupling," *IEEE Trans. Power Electron.*, vol. 30, no. 7, pp. 3998–4008, Jul. 2015.

[7] D. Patil, M. Sirico, L. Gu, and B. Fahimi, "Maximum efficiency tracking in wireless power transfer for battery charger: Phase shift and frequency control," in *Proc. IEEE Energy Convers. Congr. Expo.*, Milwaukee, WI, USA, 2016, pp. 1–8.

[8] V. Jiwariyavej, T. Imura, and Y. Hori, "Coupling Coefficients Estimation of Wireless Power Transfer System via Magnetic Resonance Coupling Using Information From Either Side of the System," *IEEE J. Emerg. Sel. Topics Power Electron.*, vol. 3, no. 1, pp. 191–200, Mar. 2015.

[9] D. Kobayashi, T. Imura, and Y. Hori, "Real-time coupling coefficient estimation and maximum efficiency control on dynamic wireless power transfer using secondary DC–DC converter," in *Proc. 41st Annu. Conf. IEEE Ind. Electron. Soc.*, Yokohama, Japan, 2015, pp. 4650–4655.

[10] X. Dai, X. Li, Y. Li, and A. P. Hu, "Maximum efficiency tracking for wireless power transfer systems with dynamic coupling coefficient estimation," *IEEE Trans. Power Electron.*, vol. 33, no. 6, pp. 5005–5015, Jun. 2018.

[11] M. Fu, H. Yin, M. Liu, and C. Ma, "Loading and Power Control for a High-Efficiency Class E PA-Driven Megahertz WPT System," *IEEE Trans. Ind. Electron.*, vol. 63, no. 11, pp. 6867–6876, Nov. 2016.

[12] T. D. Yeo, D. Kwon, S. T. Khang, and J. W. Yu, "Design of maximum efficiency tracking control scheme for closed-loop wireless power charging system employing series resonant tank," *IEEE Trans. Power Electron.*, vol. 32, no. 1, pp. 471–478, Jan. 2017.

[13] Z. Huang, S. C. Wong, and C. K. Tse, "Control design for optimizing efficiency in inductive power transfer systems," *IEEE Trans. Power Electron.*, vol. 33, no. 5, pp. 4523–4534, May 2018.

[14] D. Ahn, S. Kim, J. Moon, and I. K. Cho, "Wireless power transfer with automatic feedback control of load resistance transformation," *IEEE Trans. Power Electron.*, vol. 31, no. 11, pp. 7876–7886, Nov. 2016.

[15] X. Tang, J. Zeng, K. P. Pun, S. Mai, C. Zhang, and Z. Wang, "Low-cost maximum efficiency tracking method for wireless power transfer systems," *IEEE Trans. Power Electron.*, vol. 33, no. 6, pp. 5317–5329, Jun. 2018.

[16] M. Kiani, B. Lee, P. Yeon, and M. Ghovanloo, "A Q-modulation technique for efficient inductive power transmission," *IEEE J. Solid-State Circuits*, vol. 50, no. 12, pp. 2839–2848, Dec. 2015.

[17] L. Yuan, B. Li, Y. Zhang, F. He, K. Chen, and Z. Zhao, "Maximum efficiency point tracking of the wireless power transfer system for the battery charging in electric vehicles," in *Proc. 18th Int. Conf. Electr. Machines Syst.*, Pattaya, Thailand, 2015, pp. 1101–1107.

[18] W. Zhong and S. Y. R. Hui, "Charging time control of wireless power transfer systems without using mutual coupling information and wireless communication system," *IEEE Trans. Ind. Electron.*, vol. 64, no. 1, pp. 228–235, Jan. 2017.

[19] T. Diekhans and R. W. De Doncker, "A dual-side controlled inductive power transfer system optimized for large coupling factor variations and partial load," *IEEE Trans. Power Electron.*, vol. 30, no. 11, pp. 6320–6328, Nov. 2015.

[20] A. Berger, M. Agostinelli, S. Vesti, J. A. Oliver, J. A. Cobos, and M. Huemer, "A wireless charging system applying phase-shift and amplitude control to maximize efficiency and extractable power," *IEEE Trans. Power Electron.*, vol. 30, no. 11, pp. 6338–6348, Nov. 2015.

[21] K. Colak, E. Asa, M. Bojarski, D. Czarkowski, and O. C. Onar, "A novel phase-shift control of semibridgeless active rectifier for wireless power transfer," *IEEE Trans. Power Electron.*, vol. 30, no. 11, pp. 6288–6297, Nov. 2015.

[22] R. Mai, Y. Liu, Y. Li, P. Yue, G. Cao, and Z. He, "An active rectifier based maximum efficiency tracking method using an additional measurement coil for wireless power transfer," *IEEE Trans. Power Electron.*, vol. 33, no. 1, pp. 716–728, Jan. 2018.

[23] H. Li, J. Fang, S. Chen, K. Wang, and Y. Tang, "Pulse density modulation for maximum efficiency point tracking of wireless power transfer systems," *IEEE Trans. Power Electron.*, vol. 33, no. 6, pp. 5492–5501, Jun. 2018.

[24] H. Li, K. Wang, J. Fang, and Y. Tang, "Pulse density modulated ZVS full-bridge converters for wireless power transfer systems," *IEEE Trans. Power Electron.*, vol. 34, no. 1, pp. 369–377, Jan. 2019.

[25] Y. Lim, H. Tang, S. Lim, and J. Park, "An adaptive impedance-matching network based on a novel capacitor matrix for wireless power transfer," *IEEE Trans. Power Electron.*, vol. 29, no. 8, pp. 4403–4413, Aug. 2014.

[26] K. Silay *et al.*, "Load optimization of an inductive power link for remote powering of biomedical implants," in *Proc. IEEE Int. Symp. Circuits Syst.*, 2005, pp. 533–536.

[27] W. Zhong and S. Y. Hui, "Reconfigurable wireless power transfer systems with high energy efficiency over wide load range," *IEEE Trans. Power Electron.*, vol. 33, no. 7, pp. 6379–6390, Jul. 2018.

[28] W. Zhong and S.Y.R Hui, "Maximum energy efficiency operation of series-series resonant wireless power transfer systems using on–off keying modulation," *IEEE Trans. Power Electron.*, vol. 33, no. 4, pp. 3595–3603, Apr. 2018.

[29] D. M. Dwelley, "Voltage mode feedback burst mode circuit," U.S. Patent 6 307 356 B1, Oct. 23, 2001.

[30] "High performance resonant mode controller," ON Semiconductor, Phoenix, AZ, USA, NCP1395 A/B. Accessed: Sep. 2008. [Online]. Available: http://www.onsemi.com/pub_link/Collateral/NCP1395-D.PDF

[31] "8-pin highperformance resonant mode controller," Texas Instruments, Dallas, TX, USA, UCC25600. Accessed: Sep. 2008. [Online]. Available: http://focus.ti.com/lit/ds/symlink/ucc25600.pdf
[32] B. Wang, X. Xin, S. Wu, H. Wu, and J. Ying, "Analysis and implementation of LLC burst mode for light load efficiency improvement," in *Proc. 24th Annu IEEE Appl. Power Electron. Conf. Expo.*, Feb. 2009, pp. 58–64.
[33] Y. Jang and M. M. Jovanovic, "Light-load efficiency optimization method," *IEEE Trans. Power Electron.*, vol. 25, no. 1, pp. 67–74, Jan. 2010.
[34] W. Feng, F. C. Lee, and P. Mattavelli, "Optimal trajectory control of burst mode for LLC resonant converter," *IEEE Trans. Power Electron.*, vol. 28, no. 1, pp. 457–466, Jun. 2013.
[35] H. Zeng, N. S. González-Santini, Y. Yu, S. Yang, and F. Z. Peng, "Harmonic burst mode control strategy for full-bridge series resonant convertersfor electric vehicles application," in *Proc. IEEE Energy Convers. Congr. Expo.*, Montreal, QC, Canada, 2015, pp. 579–585.
[36] S. Chen, H. Li, and Y. Tang, "Extending the operating region of inductive power transfer systems through dual-side cooperative control," *IEEE Trans. Power Electron.*, to be published.
[37] S. C. Tang, S. Y. Hui, and H. Chung, "Evaluating the shielding effects on printed-circuit-board transformers using ferrite plates and copper sheets," *IEEE Trans. Power Electron.*, vol. 17, no. 6, pp. 1080–1088, 2002.

Wenxing Zhong (Member, IEEE) received the B.Eng. degree in electrical engineering from Tsinghua University, Beijing, China, in 2007, and the Ph.D. degree from the City University of Hong Kong, Hong Kong, in 2012.

Currently, he is a Professor with the Department of Electrical Engineering, Zhejiang University, Hangzhou, China. From March 2016 to May 2017, he was a Research Assistant Professor with the Department of Electrical and Electronic Engineering at the University of Hong Kong, Hong Kong. His research interests include wireless power transfer and power electronics.

Dr. Zhong was the recipient of two Transactions First Prize Paper Awards from IEEE Power Electronics Society.

Hao Li received the B.S. and M.S. degrees from Zhejiang University, Hangzhou, China, in 2017 and 2020, respectively, all in electrical engineering.

His research interests include wireless power transfer technologies.

S. Y. R. Hui (Fellow, IEEE) received the B.Sc. degree (hons.) in electrical and electronic engineering from the University of Birmingham, Birmingham, U.K., in 1984, and the D.I.C. and Ph.D. degrees in electrical engineering from the Imperial College London, London, U.K., in 1987.

Currently, he holds the Philip Wong Wilson Wong Chair Professorship at the University of Hong Kong, Hong Kong, and a Chair Professorship at the Imperial College London. He has authored or coauthored over 450 research papers including 270 refereed journal publications. Over 60 of his patents have been adopted by industry. His research interests include power electronics, wireless power, sustainable lighting and smart grid. His inventions on wireless charging platform technology underpin key dimensions of Qi, the world's first wireless power standard, with freedom of positioning and localized charging features for wireless charging of consumer electronics. He also developed the Photo-electro-thermal Theory for LED systems.

Dr. Hui is a fellow of the Australian Academy of Technological Sciences and Engineering, US National Academy of Inventors, and Royal Academy of Engineering U.K. He was the recipient of the IEEE Rudolf Chope R&D Award and the IET Achievement Medal (The Crompton Medal), in 2010, and the IEEE William E. Newell Power Electronics Award, in 2015.

Mark Dehong Xu (Fellow, IEEE) received the Ph.D. degree from the Department of Electrical Engineering, Zhejiang University, China, in 1989.

He has been a Full Professor with Zhejiang University, Hangzhou, China, since 1996. He was a Visiting Professor with the Department of Electrical Engineering at University of Tokyo of Japan, from May 1995 to June 1996; with the Center of Power Electronics System at Virginia Tech, Blacksburg, VA, USA, from June to December 2000; and with the Power Electronics Lab of ETH in Zurich, Switzerland, from February to April of 2006. He has authored ten books and more than 200 IEEE Journal or Conference papers. He holds more than 40 patents. His research interests include power electronics topology, control, and applications to renewable energy and energy efficiency.

Dr. Xu is at-large Adcom Member of IEEE Power Electronics Society during 2020–2022. He was the recipient of six IEEE Transaction or Conference Prize Paper Awards. He was the recipient of the IEEE Power Electronics Society (PELS) R. D. Middlebrook Achievement Award, in 2016. He was the IEEE PELS Distinguished Lecturer, from 2015 to 2018. He is Co-Editor-in-Chief for IEEE Open Journal of Power Electronics, an Associate Editor for IEEE Transaction on Power Electronics, etc. He was the General Chair of IEEE International Symposium on Industrial Electronics (ISIE2012, Hangzhou), IEEE International Symposium on Power Electronics for Distributed Generation Systems (PEDG2013, Arkansas), IEEE International Power Electronics and Applications Conference (PEAC2018, Shenzhen), etc.